Advances in Water Resources 37 (2012) 73–85

Contents lists available at SciVerse ScienceDirect

Advances in Water Resources

journal homepage: www.elsevier.com/locate/advwatres

Experimental and computational investigation of local scour around bridge piers

Ali Khosronejad, Seokkoo Kang, Fotis Sotiropoulos *

Saint Anthony Falls Laboratory, University of Minnesota, 2 Third Ave. SE, Minneapolis, MN 55414, United States

ARTICLE INFO

Article history:
Received 5 May 2011
Received in revised form 27 September 2011
Accepted 27 September 2011
Available online 25 November 2011

Keywords:
Bridge pier
Turbulent flow
Local scour
Immersed boundary method
Numerical modeling
Sediment transport

ABSTRACT

Experiments and numerical simulations are carried out to study clear-water scour around three bridge piers with cylindrical, square, and diamond cross-sectional shape, respectively. To handle movable-bed channels with embedded hydraulic structures, the fluid–structure interaction curvilinear immersed boundary (FSI-CURVIB) method is employed. The hydrodynamic model solves the unsteady Reynolds-averaged Navier–Stokes (URANS) equations closed with the k-ω turbulence model using a second-order accurate fractional step method. Bed erosion is simulated by solving the sediment continuity equation in the bed-load layer using a second-order accurate unstructured, finite-volume formulation with a sand-slide, bed-slope-limiting algorithm. Grid sensitivity studies are carried out to investigate the effect of grid resolution on the predictive capability of the model. Comparisons of the simulations with the experimental data show that for all three cases the agreement is reasonable. A major finding of this work, however, is that the predictive capability of the URANS morphodynamic model improves dramatically for the diamond shape pier for which sediment transport is driven primarily by the shear layers shed from the pier sharp edges. For piers with blunt leading edge, on the other hand, as the circular and square shapes, the URANS model cannot resolve the energetic horseshoe vortex system at the pier/bed junction and thus significantly underpredicts both the scour depth at the nose of the pier and the rate of scour growth. It is also shown that ad hoc empirical corrections that modify the calculated critical bed shear stress to enhance scour rate in the pier leading edge need to be applied with caution as their predictive capabilities are not universal but rather depend on the pier shape and the region of the flow.

1. Introduction

Flows around hydraulic structures in natural mobile-bed channels are characterized by arbitrary geometric complexity, due to the inherent morphologic richness of bed bathymetry and a wide variety of hydraulic structures (e.g. barbs, bridge piers, abutments, spur-dikes, etc.), and are dominated by energetic coherent vortical structures. Such vortices interact with sediments on the bed leading to local scour, which could endanger streambed stability and undermine the structural reliability of embedded hydraulic structures. Local scour is one of the major failure modes of bridge piers. Briaud et al. [7], for instance, report that as of 1999 more than 1000 of about 600,000 bridges in the United States failed with 60% of these failures being due to scour. Furthermore, local scour could be an important factor in the design of offshore wind and hydrokinetic turbine farms. According to Sumer [52] the cost of a wind turbine foundation in environments where scour protection is a key design issue could be more than 30% of the total turbine design and installation cost.

The role of unsteady coherent vortices as the primary mechanism for initiating scour around bridge foundations is well established and documented in several previous studies. Baker [5] was among the first to visualize the turbulent horseshoe vortex system (THSV) that develops in the upstream junction of a cylindrical pier with a flat, rigid bed for Reynolds numbers up to 90,000 (based on the pier diameter D and the approach flow velocity) and was able to identify primary and secondary vortical structures wrapping around the pier. Dargahi [9] employed a visualization technique based on hydrogen bubbles to also study the flow around a cylindrical pier on a flat rigid bed. His experiments revealed the presence of an intricate THSV system consisting of up to five highly energetic necklace-like vortical structures in the front of the cylindrical pier, which appeared to form, interact with each other and merge in a periodic or quasi-periodic manner. In a follow-up study Dargahi was the first to study and describe qualitatively the flow patterns upstream of the pier mounted on a mobile bed along with the initiation and progression toward equilibrium of the scour process [10]. Several other experimental studies focusing on the dynamics of the THSV system for cylindrical piers on a flat rigid bed have also been reported by Devenport and Simpson [11], Agui and Andreopoulos [2], Doligalski et al. [13] and Seal and Smith [49]. Martinuzzi and Tropea [32] and Hussein and Martinuzzi

* Corresponding author.
E-mail address: fotis@umn.edu (F. Sotiropoulos).

0309-1708/$ - see front matter © 2011 Elsevier Ltd. All rights reserved.
doi:10.1016/j.advwatres.2011.09.013

[22] have also studied the flow field around other pier-like geometries with square and rectangular cross-sections mounted on a flat rigid bed. Dey et al. [12], Graf and Istiarto [20], and Roulund et al. [47] investigated mean flow and turbulence kinetic energy distribution inside the equilibrium scour hole around cylindrical piers. A recent comprehensive study was reported by Unger and Hager [54] who carried out particle image velocimetry (PIV) experiments of bridge pier flows over a wide range of Reynolds numbers. They found that a strong downward flow in the front of the cylinder and the THSV are the main culprits for the initiation and subsequently growth of the scour hole. They also reported that the primary contribution to local scour occurs in the region situated in front of the pier where the flow is dominated by the energetic THSV system.

In addition to the several experiments, a number of computational studies have also been reported in the literature. Most of these studies have focused on the flow patterns on a flat rigid bed but several of them have also reported results for mobile bed cases. Computational studies using unsteady Reynolds-averaged Navier–Stokes (URANS) models by focusing on flow patterns around piers on a flat rigid bed have been reported by Mendoza-Cabrales [34], Richardson and Panchang [45], Tseng et al. [53], Nurtjahyo [36], Ge and Sotiropoulos [17], and Salaheldin et al. [48]. URANS models are, in principle, capable of resolving periodic, large-scale vortex shedding from hydraulic structures and have yielded promising results in simulating turbulence past very complex bridge pier geometries (e.g. Ge and Sotiropoulos[17]). However, it should be noted that the two-equation isotropic eddy viscosity turbulence models that are typically used to close the URANS equations tend to overpredict the magnitude of the eddy viscosity at the junction of the bridge foundation with the bed and could, thus, suppress and significantly underpredict the intensity of the all important for scour initiation THSV system [17,57,45,3].

To overcome the inherent limitations of URANS models, researchers have employed hybrid, integrating URANS and Large-Eddy Simulation (LES), and LES models to simulate the THSV dynamics past hydraulic structures. Paik and Sotiropoulos [42,43] were the first to apply the detached-eddy simulation (DES) approach, a hybrid URANS/LES model, to simulate the dynamics of large-scale coherent vortices past a bridge abutment and the cylindrical wing-shaped pier studied experimentally by Deveport and Simpson [11]. They showed that DES can capture the rich dynamics of coherent vortices induced by hydraulic structures, reproduced the experimentally documented bi-modal fluctuations of the THSV, and explained the underlying physical mechanisms that give rise to such complex unsteady phenomena. Escauriaza and Sotiropoulos [14] recently applied the same DES approach to study the dynamics of the flow past the cylindrical pier mounted on a flat rigid bed studied experimentally by Dargahi [10] and obtained results in good agreement with the experimental observations. Several other studies have also been reported employing LES and DES, which have further reinforced the experimental observations and shed new insights into several aspects of the coherent dynamics of flows past hydraulic structures [53,8,40,14,30,31,28,29]. In a number of these studies simulations have been carried out for bridge foundations on mobile beds but with the shape of the bed frozen and prescribed from experimental measurements at equilibrium [30,31,41]. LES and DES simulations have been shown to reproduce correctly the dynamics of large-scale vortices past bridge foundations and accurately predict the turbulence levels produced by these large-scale organized motions (e.g. Paik et al. [41]). Using such methods, however, to develop engineering models of sediment transport and scour is challenging due to the excessive computational resources required. It is well known for instance that the time-scale of scour to approach equilibrium is much larger than the time scale of turbulence fluctuations-the former being of the order of hours or days while the latter are of the order of seconds or smaller. Such disparity in temporal scales makes coupled hydro-morphodynamic simulations of scour using LES or DES impractical for engineering calculations. For that most previous work on numerical prediction of scour have employed RANS or URANS turbulence models, which are far more economical than LES or DES.

Olsen and Melaaen [39] and Olsen and Kjellesvig [38] carried out the first 3D steady RANS, coupled hydro-morphodynamics numerical calculations of flow and scour around a cylindrical pier mounted on a bed covered with mobile, non-cohesive material in order to predict the local scour on the non-cohesive sediment materials for clear-water scour regime. Roulund et al. [47] and Nagata et al. [35] also simulated the flow and local scour process around wall-mounted vertical cylinders using URANS models under live bed condition. Escauriaza and Sotiropoulos [14] where the first to explore the dynamics of scour using DES to simulate the flow past a cylindrical bridge pier coupled with a Lagrangian model of bed load transport. These simulations were not intended to predict the growth of scour and its approach to equilibrium but rather to elucidate the Lagrangian dynamics during the initial stages of the phenomenon. Their results shed new fundamental insights into the problem by showing that phenomena that have been shown to characterize scour initiation under clear-water conditions in the laboratory (such as intermitency, saltation, sliding and near-wall streak formation) can be captured by a Lagrangian model that is based on a coherent-structure resolving hydrodynamic model. In addition, Escauriaza and Sotiropoulos [14] showed that the bed-load flux exhibits multi-fractal scaling. In a more recent study, Escauriaza and Sotiropoulos [15] developed a coupled hydro-morphodynamic model using DES and the Arbitrary Lagrangian Eulerian approach to simulate bed deformation. They solved the Exner equation coupled with a novel transport equation for calculating the instantaneous sediment velocity field in the bed-load layer, which was based on the Lagrangian model developed earlier by the same authors [14]. Escauriaza and Sotiropoulos [15] applied their model to simulate the evolution of scour in the vicinity of the cylinder studied experimentally by Dargahi [10] and showed that the model was able to capture the growth and propagation of bed-forms within and around the scour hole with physically realistic statistical properties. Due to the long computational times required by their model, however, Escauriaza and Sotiropoulos [15] reported simulations for only the initial stages of the scouring process.

The objective of this paper is twofold: (1) to extend a recently developed method for coupled hydro-morphodynamics simulations in arbitrarily complex domains to flows past hydraulic structures [26]; and (2) systematically investigate the predictive capabilities of the URANS approach for various bridge-pier geometries. The governing equations are solved in a background Cartesian or curvilinear mesh that does not conform to the shape of embedded solid boundaries (e.g. the bed of a natural stream, embedded hydraulic structures, etc.) using the curvilinear immersed boundary (CURVIB) method [19,18,26]. The method was extended to simulate bed morphodynamics by Khosronejad et al. [26]. The sediment transport model considers only bed load transport and turbulence is modeled using the URANS equations closed with the k-ω model [56] with wall functions. The dynamically evolving shape of the sediment/water interface, which, as required by the CURVIB method, is discretized with an unstructured triangular mesh, is calculated by solving the non-equilibrium sediment mass balance equation in the bed-load layer, the so-called Exner-Polya equation [50], using the numerical approach developed by Khosronejad et al. [23]. To facilitate the validation of the numerical model for flows in channels with embedded hydraulic structures, in this work we also carry out a series of laboratory experiments using cylindrical, square and diamond-shaped piers mounted in

rectangular flume with mobile bed. Calculations are carried out for all cases studied experimentally and the computed results are compared with the experimental data in terms of both the temporal evolution of maximum scour and equilibrium bed elevation. A grid sensitivity study is also carried out to investigate the relative importance of numerical errors due to the discretization of the governing equations and turbulence closure modeling assumptions in the overall predictive capabilities of the numerical method.

In what follows, we first briefly present the hydrodynamic and morphodynamic models. Subsequently we present the laboratory experiments we carried out to collect bed elevation data to validate the numerical simulations. This is followed by the presentation and discussion of the simulation results for the three test cases we consider in this work (cylindrical, square and diamond shaped piers) to investigate the predictive capability of the URANS model in simulations of local scour past bridge piers. We also present and discuss the results of a grid refinement study for each test case. In addition, we present the results of an investigation seeking to explore the predictive capabilities and physical consistency of previously proposed empirical formulas that attempt to modify in an ad hoc manner the shear stress at the leading of the pier to improve the predictions of URANS scour models [23,60]. Finally, we summarize the main contribution of this work and discuss modeling challenges that still remain in the numerical simulation of local scour processes around bridge pier hydraulic structures using URANS based models.

2. The hydrodynamic model

2.1. Governing equations

The hydrodynamic model solves numerically the three-dimensional, incompressible, URANS and continuity equations closed with the k-ω model [56]. The governing equations are non-dimensionalized using the bulk velocity U and a characteristic length scale (equal to the flow depth H in this study) as the velocity and length scales, respectively. The governing equations for the mean flow are formulated in generalized curvilinear coordinates using the full-transformation formulation proposed by Ge and Sotiropoulos [18] as follows. Using tensor notation (repeated indices imply summation) the transformed equations read as follows:

$$J\frac{\partial U^j}{\partial \xi^j}=0 \tag{1}$$

$$\frac{1}{J}\frac{\partial U^i}{\partial t}+\frac{\xi^i_{x_\varrho}}{J}\left(\frac{\partial}{\partial \xi^j}(U^j u_\varrho)+\frac{\partial}{\partial \xi^j}\left(\frac{\xi^j_{x_\varrho}p}{J}\right)-\frac{1}{Re}\frac{\partial}{\partial \xi^j}\left(\frac{g^{jk}}{J}\frac{\partial u_\varrho}{\partial \xi^k}\right)+\frac{\partial \tau_{\varrho j}}{\partial \xi^j}\right)=0 \tag{2}$$

where $\{x_i\}$ and $\{\xi^i\}$ are the Cartesian and generalized coordinates (i = 1,2, and 3), respectively, J is the Jacobian of the geometric transformation $J=\partial(\xi^1,\xi^2,\xi^3)/\partial(x_1,x_2,x_3)$, $\xi^i_{x_\varrho}=\partial\xi^i/\partial x_\varrho$ are the metrics of the geometric transformation, $\{u_\varrho\}$ are the Cartesian velocity components, $U^i=\xi^i_{x_m}u_m/J$ are the contravariant components of the volume flux vector, $g^{jk}=\xi^j_{x_\varrho}\xi^k_{x_\varrho}$ are the components of the contravariant metric tensor, p is the pressure, τ_{ij} is the Reynolds stress of RANS models, and Re is the Reynolds number defined as $Re=\frac{UH}{\nu}$ in which $\nu$is fluid kinematic viscosity.

The governing equations for the k-ω model [56] read in generalized curvilinear coordinates as follows [24]:

$$\frac{1}{J}\frac{\partial(\rho k)}{\partial t}+\frac{\partial}{\partial \xi_j}(\rho k U_j)=\tau_{ij}\frac{\xi^k_j}{J}\frac{\partial u_i}{\partial \xi_k}-\frac{1}{J}\beta^*\rho k\omega+\frac{\partial}{\partial \xi_j}\left((\mu+\sigma^*\mu_t)\frac{g^{jk}}{J}\frac{\partial k}{\partial \xi_k}\right) \tag{3}$$

$$\frac{1}{J}\frac{\partial(\rho \omega)}{\partial t}+\frac{\partial}{\partial \xi_j}(\rho \omega U_j)=\alpha\frac{\rho\omega}{k}\tau_{ij}\frac{\xi^k_j}{J}\frac{\partial u_i}{\partial \xi_k}-\frac{1}{J}\beta\rho\omega^2+\frac{\partial}{\partial \xi_j}\left((\mu+\sigma^*\mu_t)\frac{g^{jk}}{J}\frac{\partial \omega}{\partial \xi_k}\right) \tag{4}$$

$$\mu_t=\rho k/\omega \tag{5}$$

where μ_t is the dynamic eddy viscosity, ρ is the density, and the closure coefficients are given as α = 5/9, β = 3/40, β^* = 9/100, and σ^* = 1/2. The components of the Reynolds stress tensor in Eq. (2) are calculated using the Boussinesq hypothesis as follows:

$$\tau_{ij}=-2\mu_t S_{ij}+\frac{2}{3}\rho k\delta_{ij} \tag{6}$$

where S_{ij} is the Reynolds averaged strain-rate tensor.

2.2. The CURVIB flow solver

The details of the numerical method for solving the mean flow and turbulence closure governing equations have already been documented extensively elsewhere [18,6,24] and only a brief summary of key elements of the method will be given here.

The governing equations are discretized in space on a hybrid staggered/non-staggered grid arrangement [19,18] using the second-order accurate QUICK scheme for the convective terms along with second-order accurate, three-point central differencing for the divergence, pressure gradient and viscous-like terms. The time derivatives are discretized using second-order backward differencing [24].

The discrete mean flow equations are integrated in time using an efficient, second-order accurate fractional step methodology coupled with a Jacobian-free, Newton–Krylov solver for the momentum equations and a GMRES solver enhanced with multigrid as preconditioner for the Poisson equation. For more details the reader is referred to [18,6,24].

Geometrically complex computational domains are handled using the sharp-interface CURVIB method [18], which was recently extended by Khosronejad et al. [26] to enable coupled hydro-morphodynamic simulations. To facilitate a brief description of the method in the context of the present work, consider a straight open channel with a layer of mobile sediment covering the channel bed and an embedded hydraulic structure, like a bridge pier, mounted on the bed (see Fig. 1). It should be noted that even though we focus herein on straight open channels, the method is general and readily applicable to simulate flows in natural meandering waterways (see Kang et al. [24,25]). The background computational domain consists of a straight channel that outlines the actual channel but is sufficiently deep to contain entirely the sediment/water interface at all times. The computational domain is discretized with a boundary-fitted curvilinear mesh, so that meandering open channels can also be handled. The sediment/water interface and embedded bridge pier are discretized with unstructured grids immersed in the background domain and treated as sharp-interfaces in accordance with the CURVIB formulation. Note that for the sake of our discussion we assume for the time being that the sediment/water interface is fixed; the method for calculating the deformation of the bed and its interaction with the flow will be discussed in the subsequent section. According to the CURVIB formulation, the governing equations are solved at the background grid nodes in the fluid phase (fluid nodes) with boundary conditions specified at fluid nodes in the immediate vicinity of the sediment/water and bridge pier/water interfaces (denoted as immersed boundary (IB) nodes). All nodes inside the sediment layer and bridge pier domains (denoted as external nodes) are blanked out from the computation. Boundary conditions for the velocity components and turbulence quantities are reconstructed at all IB nodes using the wall modeling approach within the CURVIB framework (see next section). The efficient ray-tracing algorithm developed by Borazjani et al. [6] is applied to re-classify the grid nodes every time when the bed geometry changes due to local scour.

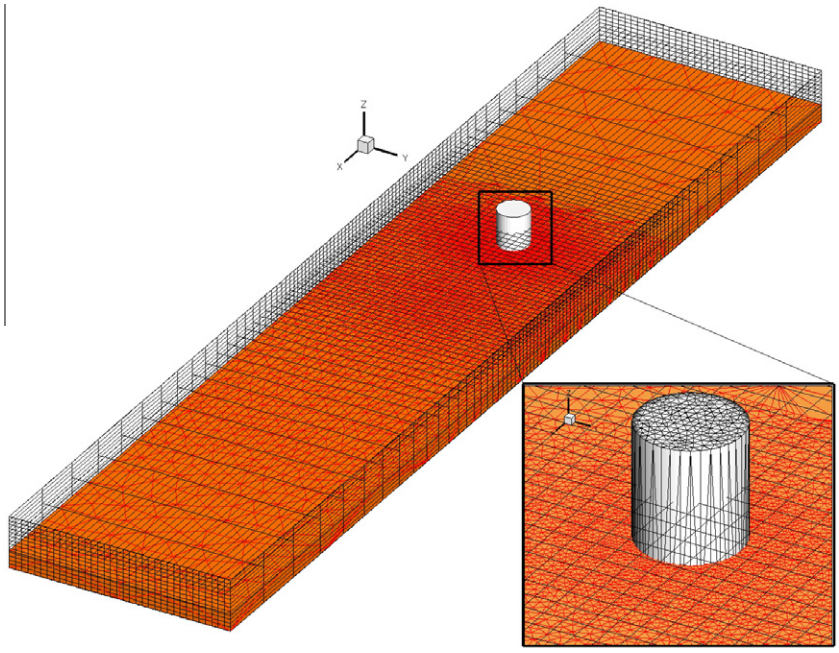

Fig. 1. Typical view of the CURVIB grid system used for the flow domain (structured grid in black), pier body (unstructured mesh in grey), and sediment layer (unstructured grid in red). (For interpretation of the references to colour in this figure legend, the reader is referred to the web version of this article.)

The following wall modeling approach is adopted to reconstruct the velocity components at IB nodes and the bed shear stress on bed surface [27]:

$$\frac{U}{u_*} = \begin{cases} y^+ & y^+ \leqslant y_o^+ \\ \frac{1}{\kappa}\ln(Ey^+) & y^+ > y_o^+ \end{cases} \tag{7}$$

where U is the velocity magnitude at the nearest node to the wall boundary (located at distnace y off of the wall), $y^+ \left(=\frac{yu_*}{\upsilon}\right)$ is non-dimensional distance in wall units, u_* is the shear velocity, κ is the von Karaman constant, $y_o^+ = 11.53$ [27], and E is the roughness parameter, which is related to the roughness Reynold number $k_s^+ = u_* k_s/\upsilon$ as follow [27]

$$E = \exp[\kappa(B - \Delta B)] \tag{8}$$

where k_s is the effective roughness height of the wall boundary, B is additive constant = 5.2. ΔB is the roughness function which reads as follows [27]:

$$\Delta B = \begin{cases} 0 & k_s^+ < 2.25 \\ \left[B - 8.5 + \frac{1}{\kappa}\ln\left(k_s^+\right)\right] & \\ \quad \times \sin\left[0.4258\left(\ln k_s^+ - 0.811\right)\right] & 2.25 < k_s^+ < 90 \\ B - 8.5 + \frac{1}{\kappa}\ln\left(k_s^+\right) & k_s^+ \geqslant 90 \end{cases} \tag{9}$$

The effective roughness height k_s plays an important role in quantifying the influence of roughness on the bed and solid boundaries (i.e. side walls and bridge pier structures). Theoretically, for a stationary flat bed in real waterways k_s should be equal to the median grain size d_{50}. In practice, however, for mobile beds somewhat higher values are adopted [59]. In the present mobile bed simulations we employ a value of $k_s = 3d_{50}$ for the bed and treat the side walls and bridge pier structures as hydraulically smooth surfaces.

Finally, it is important to mention that the CURVIB solver is fully parallelized using the message passing interface (MPI) communication standard to run on parallel high-performance clusters.

3. The bed morphodynamic model

We describe herein the bed morphodynamic model developed by Khosronejad et al. [26]. In its present form the model is only applicable for cases for which all sediment transport occurs in bed load mode within a live layer of thickness δ_{BL} (set equal to $2d_{50}$) just above the bed (the bed is located at elevation z_b above a datum level). The temporal variation of the bed elevation is governed by the sediment continuity equation, the so-called Exner-Polya equation [44], which reads as follows:

$$(1-\gamma)\frac{\partial z_b}{\partial t} = -\nabla \cdot \mathbf{q}_{BL} \tag{10}$$

where γ is sediment material porosity, ∇ denotes the divergence operator, and $\mathbf{q}_{BL}$ is the bed load flux vector.

Since in the CURVIB method the bed is meshed by an unstructured triangular grid, Eq. (10) is discretized and solved using a finite volume method suitable for unstructured grids. Using the divergence theorem, Eq. (10) can be discretized at a given triangular element on the bed as follows [26]:

$$(1-\gamma)\frac{\Delta z_b}{\Delta t} = -\frac{1}{A_h}\sum_{i_e=1,2,3}\left[\mathbf{q}_{BL}\cdot(d\mathbf{s}\times\delta_{BL})\right]_{i_e} = -\frac{1}{A_h}\sum_{i_e=1,2,3}\left[\mathbf{q}_{BL}\cdot\mathbf{n}\right]_{i_e} \tag{11}$$

where Δz_b is the bed elevation change over time step Δt, A_h is the projection of triangle bed cell area on horizontal plane or horizontal projected area of cell face, the summation is carried out over the three edges of the triangular element ($i_e = 1,2,3$), $d\mathbf{s}$ is the vector along a cell edge with length equal to the edge length, δ_{BL} is the vertical vector along *z-axis* with length equal to bed load layer thickness δ_{BL}, $\mathbf{n}$ ($=d\mathbf{s}\times\delta_{BL}$) is the unit normal vector to the cell face edge. The bed load flux vector $\mathbf{q}_{BL}$ is calculated as follows [26]:

$$\mathbf{q}_{BL} = \psi\|d\mathbf{s}\|\delta_{BL}\mathbf{u}_{BL} \tag{12}$$

where ψ is the local non-equilibrium sediment concentration on the bed, $\|d\mathbf{s}\|$ is the length of edge i_e, and $\mathbf{u}_{BL}$ is the flow velocity vector parallel to the bed surface both at the edge of the bed-load layer. The calculated velocity vector and bed shear stress (and

correspondingly the sediment concentration) are projected onto the cell centroid at the edge of the bed-load layer by applying the law of the wall [26]. The bed load flux $\mathbf{q}_{BL}$ at the cell face is then calculated using the GAMMA scheme (for more details see Khosronejad et al. [26]). The non-equilibrium bed concentration ψ is computed at each cell center on the bed as follows:

$$\psi = 0.015\frac{d_{50}}{\delta_b}\frac{T^{\frac{3}{2}}}{D_*^{\frac{3}{10}}} + \psi^* \tag{13}$$

where

$$D_* = d_{50}\left[\frac{(\rho_s-\rho)g}{\nu^2}\right]^{\frac{1}{3}} \tag{14}$$

$$T = \frac{\tau_* - \tau_{*cr}}{\tau_{*cr}} \tag{15}$$

$$\psi^* = \frac{\Delta t}{A_h\delta_{BL}}[\nabla\cdot\mathbf{q}_{BL}]^* \tag{16}$$

In the above equations: ρ and ρ_s are the fluid and sediment densities, g is the gravitational acceleration, T is the non-dimensional excess bed shear stress [55], τ_{*cr} is the critical bed shear stress, and τ_* is the bed shear stress $(=\sqrt{\rho u_*})$ with u_* calculated using Eq. (7). The first and second term on right hand side of Eq. (13) represents the deterministic equation of Van Rijn [55] for the equilibrium sediment concentration and non-equilibrium part of bed sediment concentration, respectively. The non-equilibrium part of bed sediment concentration is calculated based on the net sediment-flux into the bed cell at the previous time step. In other words, the actual (non-equilibrium) bed sediment concentration is computed as a combination of an equilibrium concentration and the net sediment flux into the bed cell of volume of $A_h\delta_{BL}$. In our model, and unlike previous studies in which the non-equilibrium transport equation of bed load is considered to account for the non-equilibrium condition in the sediment transport process [59,58], we calculate the non-equilibrium sediment concentration from the corresponding sediment concentration transport equation within the bed load layer (Eq. (13)). The characteristic length for sediment to adjust from non-equilibrium to equilibrium transport is assumed to be equal to the characteristic length of flow field (the flow depth in this study). Note that the divergence of the bed-load transport $[\nabla\cdot\mathbf{q}_{BL}]^*$ in Eq. (13) is calculated using the solution at the previous time level. The critical bed shear stress is computed using Shield's criterion for the flat bed critical bed shear stress (τ_{*c0}) and then corrected for a bed with transverse and longitudinal bed slopes (for more details see [26]).

In order to prevent the bed slope from exceeding the sediment material angle of repose, a mass-conservative sand-slide algorithm has been applied [26]. After solving the Exner-Polya equation and computing the new bed elevation, the entire bed is swept (for all the K_{max} number of bed cells) to identify bed cells at which the maximum bed slope is larger than the angle of repose. The aforementioned local slope correction procedure is then applied only to the so identified bed cells. Because a single application of this algorithm may not be sufficient to identify and correct all cells with excess slope, the algorithm is applied iteratively until all slopes are smaller than the material angle of repose. The bed sweeping sequence during each iteration of this algorithm is alternated between the upstream-to-downstream and downstream-to-upstream directions. For more details the reader is referred to [26].

4. Hydrodynamics and morphodynamics coupling

To simulate coupled hydro-morphodynamic interactions we employ a partitioned fluid–structure interaction (FSI) approach [6]. That is, we partition the problem into the fluid and sediment domains and solve the governing equations for the flow and the bed morphodynamic equation (Eq. (10)) separately in each domain accounting for the interaction of the two domains by applying boundary conditions at the sediment/water interface. More specifically, to solve the governing equations for the flow boundary conditions need to be specified at the bed, i.e. bed location and velocity, while to solve the bed change equation (Eq. (10)) the velocity components and bed shear stress from the flow domain are required to calculate the sediment fluxes (for more details on how to prescribe the boundary conditions on the two domains see [6,26]). In this work we found that the loose-coupling FSI approach to be sufficiently robust for the problems we considered and as such we employ it in all subsequent simulations. The loose-coupling flow-bed interaction method we employ is discussed in details in [26].

5. Laboratory study

We study experimentally turbulent flow in a straight open channel with a bridge pier mounted vertically on the bed and centered along the channel centerplane at 4 m downstream of the channel inlet (see Fig. 2). Three different pier geometries are investigated: a cylindrical pier with diameter of 16.51 cm; a diamond-shaped pier with width of 23.35 cm; and a square-shaped pier with edge length of 16.51 cm. The mobile-bed flume is 10 m long and has a rectangular cross-section that is 1.21 m wide and 45 cm deep. The flume contains a 20 cm deep layer of uniformly graded non-cohesive fine sand material with a mean particle diameter of d_{50} = 0.85 mm. All rigid walls including the bridge pier surface and flume side-walls are hydraulically smooth.

A series of five experiments, all under clear-water scour condition, is carried out for each of the pier geometries. For each experiment, the initial flat-bed elevation was recorded at the start of the experimental run and the flow was allowed to evolve in time until the equilibrium scour depth was reached. A high-definition digital camera was installed within each pier and used to observe the time evolution of scour and determine the final equilibrium scour depth. Using a vertical shaft, the vertical position of the camera could be adjusted so that the scouring process at different angles and elevations could be captured (see Fig. 2). The equilibrium condition is assumed to be reached when the rate of increase of scour depth does not exceed 5% of the pier diameter over a period of 12 h [33]. When this condition was met, the flow was stopped and the final equilibrium bed topography was measured at sub-millimeter accuracy with a laser range finder. Table 1 shows the various flow parameters and scour hole properties for each pier geometry. Photographs of the equilibrium scoured bed for each pier shape are presented in Fig. 3. The details of the measured bed topographies for each case are presented in subsequent sections of this paper where numerical simulations are compared with measurements.

Local scour around cylindrical and square shaped piers has already been studied experimentally in previous studies and various aspects of the underlying morphodynamics have been considered [10,47,1,23]. To the best of our knowledge, however, our work is the first to study local scour around a diamond pier shape. Because of the specific cross-sectional shape of the diamond pier, and in particular its sharp leading edge, it is reasonable to anticipate that the scour dynamics for this case should be quite different than for the blunt leading edge cylindrical and square shapes. Our results indeed show that the diamond shape leads to significantly smaller equilibrium local scour depth in front of the structure as compared to both the cylindrical and square shapes. The differences among the three shapes will be discussed in more detail in a subsequent section of this paper.

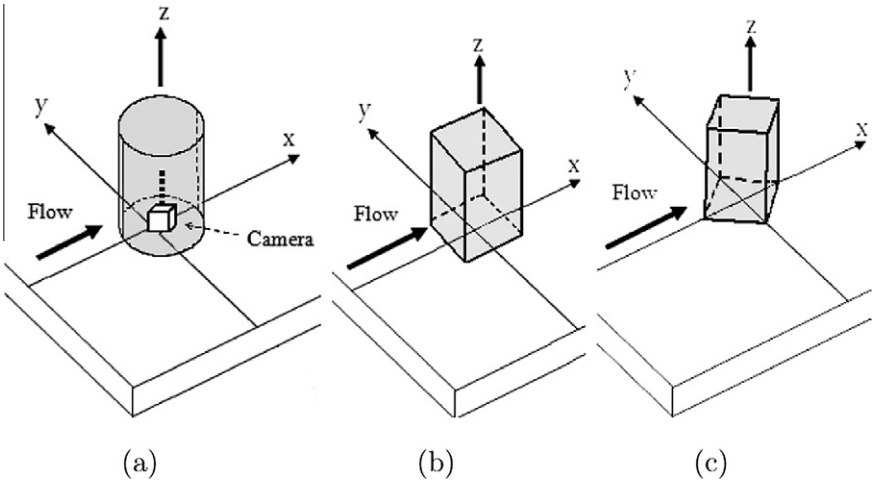

Fig. 2. Schematic of the three pier shapes studied experimentally: (a) cylinder , (b) square, and (c) diamond bridge pier geometry. The location of the digital camera mounted inside each pier to monitor local scour growth is shown in (a).

Table 1
Range of flow and scour dimensional parameters in the present the experiments. h, U_b, S_m, and d_m represent the flow depth (m), approaching flow velocity (m/s), maximum local scour depth (cm) and maximum deposition height (cm), respectively.

Pier shape	h	U_b	$Re \times 10^{-4}$	Fr	S_m	d_m
Cylinder	0.13–0.20	0.21–0.32	2.9–6.3	0.18–0.28	7.5–17.5	3.9–4.3
Diamond	0.10–0.236	0.15–0.38	3.2–4.9	0.10–0.34	9.2–19.8	3.9–4.4
Square	0.14–0.24	0.11–0.32	2.5–5.4	0.06–0.26	9.6–18.4	4.1–4.5

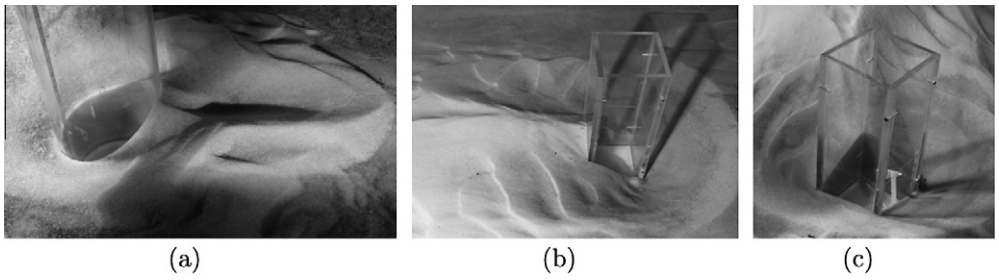

Fig. 3. Scoured bed at equilibrium for the experimental flume with (a) cylinder (Re = 46000 and Fr = 0.18 and flow is from left to the right), (b) square (Re = 30000 and Fr = 0.19 and flow is from right to the left), and (c) diamond (Re = 36000 and Fr = 0.13 and flow is from bottom to the top) bridge pier geometry.

As shown in Table 1, for the cylindrical shape the experiment was run with a bulk inflow velocity of 0.25 m/s corresponding to a uniform flow depth of 18.6 cm with a corresponding Reynolds number of Re = 46,000 and a Froude number of Fr = 0.18. The maximum scour depth for this case occurred at an angle of 45° from the upstream horizontal plane and was measured to be 6.7 cm. The equilibrium scour depth at the nose of the pier is within 94–98% of the maximum scour depth. This is to be expected since it is now well understood that for cylindrical piers (see [14]) the bimodal fluctuations of the energetic THSV could yield very high values of the instantaneous bed shear stress in the upstream junction of the pier with mobile bed causing significant scour to occur in this region. In our experiments we further observe that the scouring process begins at the side of the cylinder at an angle between 40° to 60° from the upstream horizontal plane. After nearly 5 min since the start of the flow, scour also emerges at the nose of the structure presumably due to the dominant role of the THSV. It is worthwile to note that in their recent Lagrangian computational study of sediment transport, Escauriaza and Sotiropoulos [14], found that the initiation of saltation in the bed-load layer occurs in what they referred to as "recurrent ejection events". During such an event, groups of sediment grains are lifted of the bed and travel downstream with velocities faster than the average velocity for all the other particles at the same time. Their simulations also showed that most of these events initially occur near the cylinder/bed junction at an angle approximately equal to 40° from the symmetry plane [14], which is consistent with what we observed in our experiments.

For the square shape case, the bulk inflow velocity in the experimental flume was 0.22 m/s corresponding to a uniform flow depth of 13.9 cm with a corresponding Reynolds number of Re = 30,000 and a Froude number Fr = 0.18 (see Table 1). During the early stages of the scour process (t < 5 min), scour starts at the two upstream corners of the square and these are also the two locations where the maximum scour depth (approximately equal to 7.6 cm) is observed at equilibrium. Significant scour is also observed for this case at the nose of the pier (i.e. the center of its upstream face). Depending on the Froude number, the ratio of the equilibrium scour depth at the nose of the pier to the maximum scour depth varies between 0.78 and 0.94.

Finally for the diamond shape the bulk inflow velocity in experimental flume was 0.21 m/s corresponding to a uniform flow depth of 15.7 cm with a corresponding Reynolds number of $Re = 32{,}000$ and a Froude number of $Fr = 0.17$ (see Table 1). During the early stages of bed evolution, two scour holes form at the two side corners of the pier. These are also the two locations where the maximum scour is observed at equilibrium, which is measured to be approximately 8.3 cm. In stark contrast with the other two cases, very little scour is found for this case at the sharp leading edge of the pier.

6. Numerical simulations

In this section we present the results of the numerical simulations for the three pier geometries and compare the simulations with the experiments. We carry out simulations on grids with varying resolution, ranging from 2 to 5 million grid nodes to investigate the role of numerical errors on the ability of our method to resolve the experimentally observed morphodynamics. More specifically, a major objective of our work is to identify the relative importance of numerical resolution vs. errors induced by the URANS turbulence model we employ in this work. It is well known, for instance, that URANS models cannot capture the rich dynamics of the energetic THSV at the upstream junction between the pier and the bed for cylindrical piers [46,15,30,31,41,14]. Yet, the THSV fluctuations are known to be responsible for initiating erosion and scour around piers with blunt leading edge (see extensive discussion in [15,14]). The role of the THSV, however, is not as clear for a shape like a diamond where the presence of a sharp leading edge may give rise to quite different flow patterns and scour dynamics. In this work we seek to systematically probe these important issues by considering different pier shapes and carrying out simulations on grids of varying spatial resolution.

In what follows, we first discuss various computational details. Subsequently we present and discuss the results for each case and compare with the experimental data.

6.1. Computational details

For each case, the computational domain, i.e. the rectangular open channel including the sediment layer, is discretized with a background Cartesian grid that is stretched near the side walls and the region where the structure is located (see Fig. 1). The sediment/water interface and the surface of the structure are discretized with unstructured triangular mesh, as required by the CURVIB method, and embedded in the background Cartesian mesh. The resolution of the unstructured mesh is for all cases comparable to the resolution of the background mesh as required for the accurate implementation of the CURVIB method (see Khosronejad et al. [26] for details).

For each case, we employ three, successively finer, background computational grids denoted as grids A (coarsest), B, and C (finest). The subscripts c, s, and d are used with each grid to identify the cylinder, square and diamond shaped piers, respectively. The details of the various computational grids, including number of grid nodes, near wall spacings, number of unstructured grid nodes for the immersed boundaries, and time increments are summarized in Tables 2–4.

Table 2
Computational parameters used for the cylinder case. y^+ is the minimum near-wall grid spacing in wall units, N_s is the number of nodes used to discretize the unstructured triangular mesh at the sediment/water interface, and Δt is the time step.

Grid	Number of grid nodes	y^+	N_s	Δt
A_c	$301 \times 141 \times 53$	47	14710	0.05
B_c	$353 \times 161 \times 61$	41	16156	0.025
C_c	$393 \times 185 \times 69$	32	17950	0.015

Table 3
Computational parameters used for the square case. y^+ is the minimum near-wall grid spacing in wall units, N_s is the number of nodes used to discretize the unstructured triangular mesh at the sediment/water interface, and Δt is the time step.

Grid	Number of grid nodes	y^+	N_s	Δt
A_s	$241 \times 121 \times 41$	46	10500	0.05
B_s	$301 \times 161 \times 53$	35	13284	0.025
C_s	$361 \times 181 \times 61$	29	15053	0.015

Table 4
Computational parameters used for the diamond case. y^+ is the minimum near-wall grid spacing in wall units, N_s is the number of nodes used to discretize the unstructured triangular mesh at the sediment/water interface, and Δt is the time step.

Grid	Number of grid nodes	y^+	N_s	Δt
A_d	$269 \times 141 \times 53$	39	9150	0.05
B_d	$301 \times 153 \times 61$	33	11261	0.025
C_d	$341 \times 165 \times 69$	28	12852	0.015

For all test cases, time-accurate simulations were carried out and continued until the bed surface reached steady state. This was established when the L_∞ norm of the relative change of bed elevation between two successive time steps is less than 1.0% over one flow-through period.

6.2. The cylindrical pier

As discussed above, the CURVIB method handles the sediment/water interface as a sharp-interface boundary immersed in a background Cartesian or curvilinear grid. Consequently, as the bed evolves toward equilibrium some background grid nodes that were initially in the fluid domain get "buried" with sediment and blanked out of the computation while nodes that initially were in the sediment domain emerge in the fluid phase and become part of the URANS solution domain. We begin the presentation of the results by illustrating this inherent feature of the CURVIB method, which enables it to simulate arbitrarily complex open channels with embedded hydraulic structures. In Fig. 4 the calculated sediment/water interface at equilibrium for the cylinder case is superimposed with contours of mean flow velocity magnitude plotted at several horizontal planes of the background grid near the base of the cylinder. The velocity contours are plotted only at the background grid nodes which are in the fluid phase of the solution domain and this is why as z increases (from Fig. 4a–f) they tend to cover an increasingly larger portion of the horizontal plane.

In Fig. 5 we compare the computed equilibrium bed topography on the three grid systems (A_c, B_c, and C_c) with the laboratory measurements. A number of important observations can be derived from this figure. First, it is evident from the comparisons of the calculations on the three grids that no significant improvement in the computed results has been achieved by refining the mesh from A_c to C_c. The computed scour patterns on the three grids are nearly identical to each other. Some appreciable, albeit still small, differences are only observed in the calculated deposition patterns downstream of the cylinder where as the mesh is refined the maximum deposition region becomes slightly more inclined toward the horizontal plane of symmetry. The maximum calculated scour depth and deposition height vary from 6.34 cm and 4.32 cm, respectively, on grid A_c to 6.31 cm and 4.34 cm, respectively, on grid C_c. Another important observation that follows from Fig. 5 is that the computed maximum equilibrium scour depth (approximately 6.3 cm) and deposition height (approximately 4.3 cm) are

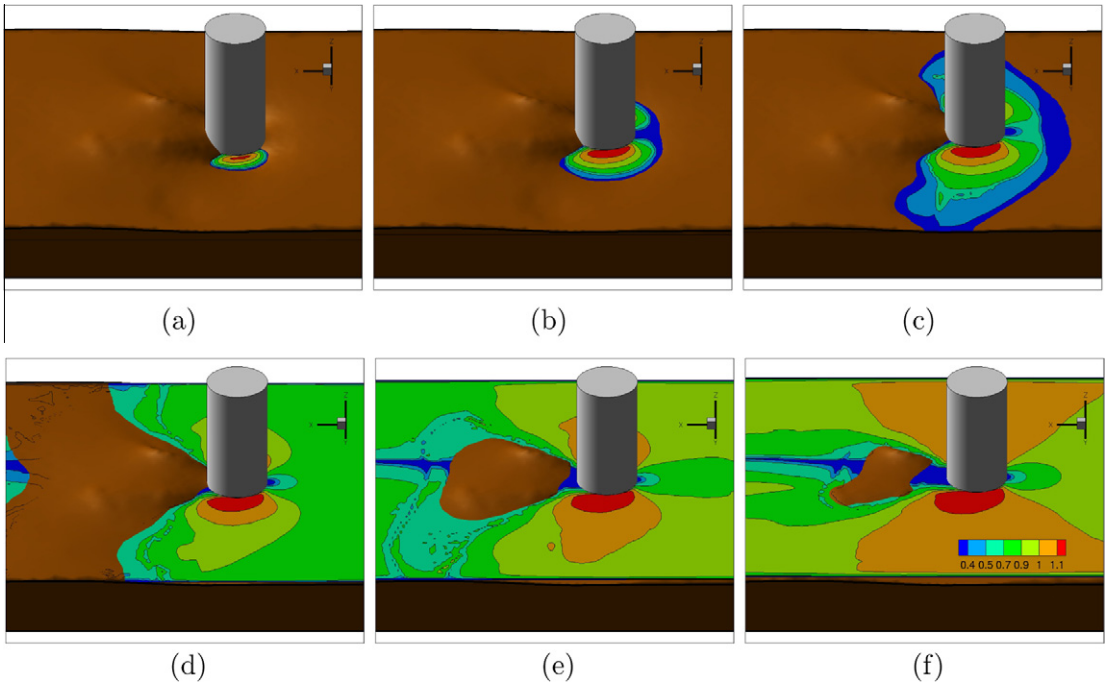

Fig. 4. Calculated equilibrium bathymetry and flow patterns for the cylinder case. Mean velocity magnitude contours are plotted at several horizontal planes located at (a) $z = -5$ cm; (b) $z = -3$ cm; (c) $z = -2$ cm; (d) $z = 0$; (e) $z = 1$ cm; and (f) $z = 3$ cm, where $z = 0$ is the location of the initial flat bed. The flow direction is from right to left.

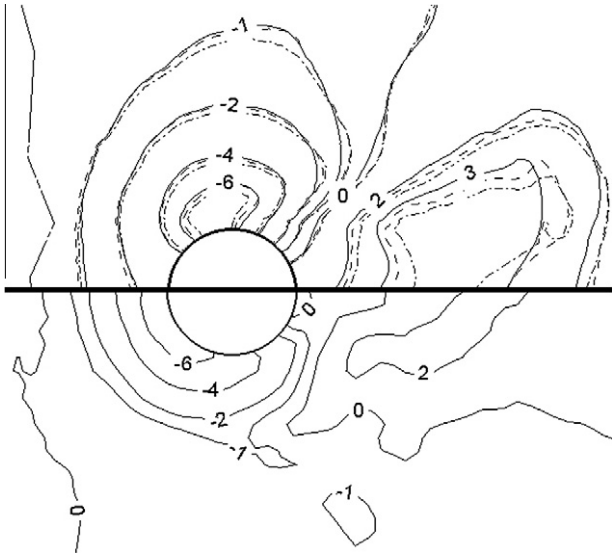

Fig. 5. Comparison of measured (bottom) and computed (top) bed topography at equilibrium (in cm). Computed results are shown for grids A_c (bold line), B_c (dashed line) and C_c (dashed-dotted line) to gauge the importance of grid refinement (see Table 2 for details of the various grids). The flow direction is from left to right.

within 6 and 5%, respectively, of the corresponding measured values of 6.7 cm and 4.1 cm. A significant qualitative difference does exist, however, between the measured and computed scour patterns. The former show a maximum scour region that wraps around the entire front half of the cylinder, starting from the pier nose and extending up until approximately 80° angle from the horizontal plane. The simulations, however, show that regardless of the density of the grid employed the maximum scour is always confined in a small pocket at the side of the cylinder. This discrepancy, which will be discussed later in more detail, should be attributed to the inherent and well known inability of URANS models to resolve the dynamics of the energetic THSV system at the upstream junction of the cylinder with the bed, which drives most of the scour in this region.

The calculated and measured time evolution of the maximum scour depth are compared in Fig. 6. This figure also shows the computed time evolution of maximum deposition height downstream of the pier on the three grid systems. As shown in Fig. 6, the bed in the experiment evolves rapidly during the first 25 min of scour. Subsequently, the rate of growth of scour slows down and the bed reaches a quasi-equilibrium state at approximately 60 min. The calculated maximum scour and deposition evolutions are identical on all three grids. The computed scour evolution is in excellent agreement with the measurements for the first 5 min of

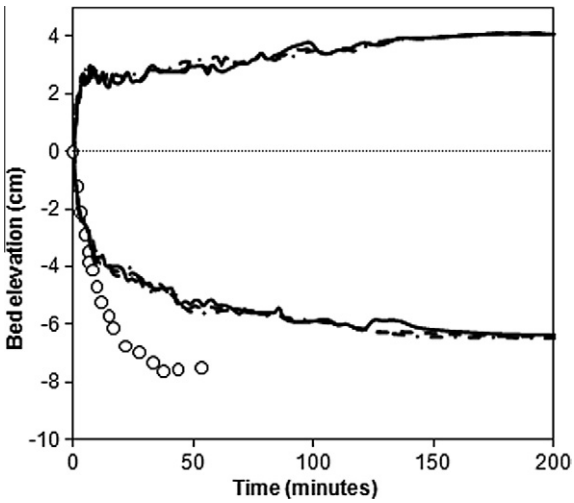

Fig. 6. Time evolution of the bed elevation around the cylindrical pier. Both the deposition (positive values) scour (negative values) levels are plotted. Circles, bold line, dashed line, and dashed-dotted line represent the measured scour depth, and computed scour depth on grids A_c, B_c, and C_c, respectively.

the process but subsequently the simulated growth rate of scour slows down significantly. As a result, for $t > 5$ min the simulated bed evolves at a much slower than measured rate and finally reaches equilibrium at approximately 180 min (i.e. at three times as long as required for equilibrium to be reached in the experiment). The reasons for the good agreement between experiments and simulations should be attributed to the different mechanisms that appear to drive the scouring process at early times. As observed in our experiments and also documented by other researchers [10,21], during the first few minutes of the process scour occurs at the sides of the pier (between angles of 45° and 90°) driven by the increase in the local bed shear stress above the critical value due to the acceleration of flow as it is directed around the pier. At later times, the THSV system grows and begins to dominate, along with the local acceleration effect, the dynamics of scour at the front part of the cylinder. As discussed above, the URANS model is not capable of resolving the dynamics of the THSV system and for that it cannot simulate the significant contribution of the THSV unsteadiness to the scouring process at later times. The URANS model, however, does reproduce the local acceleration effect at the sides of the pier, which is a kinematic effect driven by the contraction of the area available for the flow to pass due to presence of the cylinder, and for that the simulations do capture the initial stages of scour evolution during the very early stages of the process. It is notable that the fluctuations of the calculated scour depth and deposition height in Fig. 6 are induced by very large scale, periodic vortex shedding in the wake zone downstream of pier that were captured by URANS model.

6.3. The square pier

Fig. 7 compares the simulated equilibrium bed shape on all three grids with the measurements. As for the cylinder case, the three grids yield essentially identical bed bathymetry in the scour region and small discrepancies are only observed in the deposition region downstream of the pier. The calculated maximum scour depth and deposition height vary from 6.84 cm and 5.21 cm, respectively, on the coarsest grid system (grid A_s) to 6.88 cm and 5.24 cm, respectively, on the finest mesh system C_s. These values are in good agreement with the corresponding measured values of maximum scour depth 7.6 cm) and deposition height (5.5 cm). Discrepancies between experiments and simulations are observed, however, in the patterns of bed elevation contours both upstream and downstream of the pier. In the upstream region the discrepancies are similar to those observed for the cylinder case since the calculated pocket of maximum scour does not extend all the way to the symmetry plane of the pier as observed in the experiment. In the downstream region, the simulated pocket of maximum deposition is located somewhat further downstream from the pier than in the experiment.

The calculated (on all three grid systems) and measured time evolution of the maximum scour depth and the computed evolution of the maximum deposition height are shown in Fig. 8. As also observed for the cylinder case, the time evolution of scour is practically identical on all three grids and the simulations are in excellent agreement with the measurements for the first 6 min of the process. At later times ($t > 6$ min) the simulations exhibit the same underestimation of the measured rate of scour as also observed for the cylinder case. In particular, on all three grids the growth of scour slows down significantly and equilibrium is reached in about 100 min since the start of the simulation as compared to the approximately 66 minutes required to reach equilibrium in the experiment. It is worth noting, however, that in spite of the general similarities between the cylinder and square pier shapes the simulations for the latter case are in better overall agreement with the measurements than for the former case. For example, as seen in Fig. 6 for the cylinder case the simulations require nearly three times as long time as in the experiment to reach equilibrium. For the square shape, on the other hand, the simulations require only 50% more time than in the experiment to reach equilibrium. The reasons for this apparent improvement in the predictive abilities of our model insofar as the rate of scour growth is concerned is not entirely clear. We could speculate, however, that the intense shear layers that emanate from the two front corners of the square cross-section contribute to the growth of scour much more than the shear layers shed from the sides of the cylindrical shape. While for both cases the URANS model fails to capture the rich dynamics of the THSV at the nose of the pier (we discuss this more further later in the paper), the model does resolve the local increase in bed shear stress due to the shed shear layers and can thus reproduce their impact on the growth of scour. The importance of sharp edges in a pier cross-section *vis – à – vis* the growth of scour rate

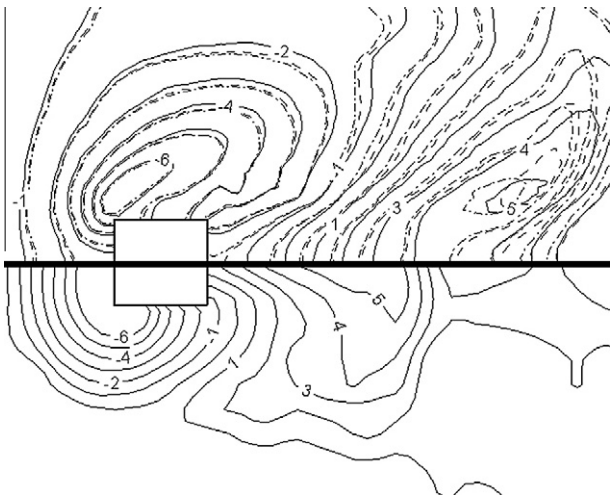

Fig. 7. Comparison of measured (bottom) and computed (top) bed topography at equilibrium (in cm). Computed results are shown for grids A_s (bold line), B_s (dashed line) and C_s (dashed-dotted line) to gauge the importance of grid refinement (see Table 3 for details of the various grids). The flow direction is from left to right.

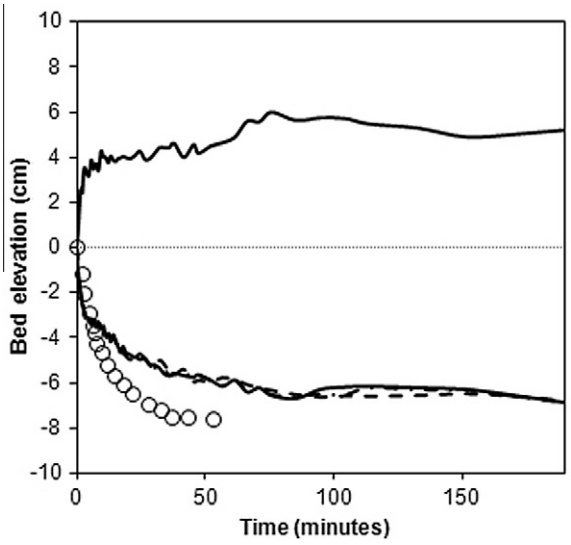

Fig. 8. Time evolution of the bed elevation around the square pier. Both the deposition (positive values) scour (negative values) levels are plotted. Circles, bold line, dashed line, and dashed-dotted line represent the measured scour depth, and computed scour depth on grids A_s, B_s, and C_s, respectively.

will be further clarified in the next section where we report the results for the diamond shape.

6.4. The diamond pier

Unlike the two previously studied cases, which involve piers with blunt nose shape, the diamond shape is not conducive to the formation of a stable THSV system due to its sharp leading edge [51]. Thus, it is reasonable to anticipate that scour in this case should primarily be driven by the two shear-layers that are shed from the two side corners of the cross-section and the local increase in bed shear stress these shear layers induce. The measured equilibrium bed elevation shown in Fig. 9 does support this conclusion. As seen in the figure, the maximum scour for the diamond shape (on all three grid systems) occurs around the two side corners and very little scour is present at the pier nose. The lack of any substantive scour at the pier nose for this case represents a significant departure from the trends we observed for both the cylindrical and square shapes for which the maximum scour region extended all the way to the pier nose.

As shown in Fig. 9, the grid refinement study shows no significant change in the predicted scour and deposition patterns. The calculated maximum scour depth and deposition height are approximately 8.5 cm and 5.2 cm, respectively. These values compare very well with the corresponding measured values of scour depth (8.3 cm) and deposition height (5.5 cm). Also the calculated bed elevation patterns are in very good overall agreement with the measurements. In fact for this case the simulations capture correctly the location of maximum scour and deposition patterns and the overall shapes of the bed elevation contours. Some differences among the three predictions and the experiments are only observed in the deposition region. These regions, however, should be attributed to the effects of the large-scale vortex shedding from the pier corners, which persists in the URANS simulations for very long times and becomes more pronounced as the grid is refined.

The calculated (on all three grids) and measured time evolution of the maximum scour depth and calculated maximum deposition height are shown in Fig. 10. In stark contrast with what we observed for the cylinder and square cases in the corresponding Figs. 6 and 8, for the diamond shape the simulations capture the measured temporal evolution of maximum scour with very good accuracy. The simulations are in excellent agreement with the measurements for the first 30 min of the process. For later times the simulated scour rate slows down somewhat compared to the measurements reaching equilibrium after approximately 100 min compared to nearly 75 min in the measurements. At all instants in time, however, the simulated instantaneous values of maximum

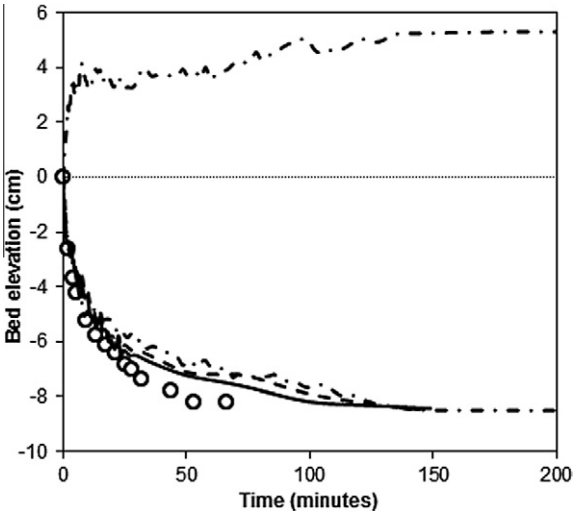

Fig. 10. Time evolution of the bed elevation around the diamond pier. Both the deposition (positive values) scour (negative values) levels are plotted. Circles, bold line, dashed line, and dashed-dotted line represent the measured scour depth, and computed scour depth on grids A_d, B_d, and C_d, respectively.

scour depth are at most within 10% of the corresponding measured value at the same instant in time. This good overall agreement between the numerical simulations and the measurements for this case further reinforce our previous comments regarding the diminished role of the THSV system as a dominant scour mechanism for the diamond pier case.

6.5. Assessment of empirical modifications of bed shear stress

The results we presented above underscore the limitations of URANS morphodynamic models in predicting the growth of scour at the leading edge of blunt piers. The reasons for this have already been discussed in detail and are linked to the inability of the URANS models to resolve the energetic fluctuations of the THSV and the so-induced large instantaneous increments of the bed shear stress in a region where the mean shear stress is very small. To mitigate this shortcoming of URANS models, some researchers have proposed and employed empirical modifications, which increase the effective bed shear stresses (τ_e) in the region of the pier nose in an ad hoc manner to capture the depth of scour hole in this region. For instance, Wu et al. [60] have used the following relation to compute an effective bed shear stress to be used in Eq. (15) in place of τ_*:

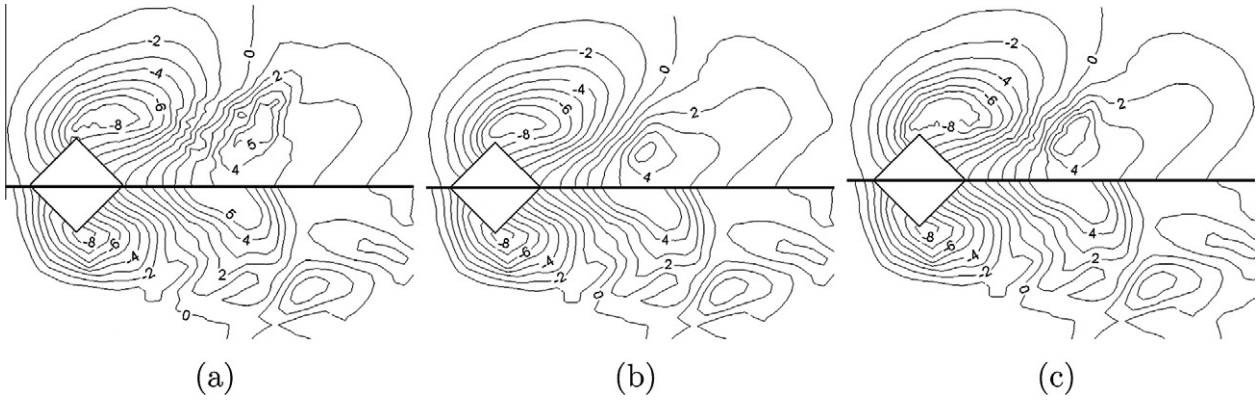

Fig. 9. Comparison of measured (bottom) and computed (top) bed topography at equilibrium (in cm). Computed results are shown for grids A_d (a), B_d (b) and C_d (c) to gauge the importance of grid refinement (see Table 4 for details of the various grids). Flow direction is from left to right.

$$(\tau_*)_e = \alpha_t \cdot Max\left\{\tau_*, \beta_t \frac{\partial z_w}{\partial s}\right\} \quad (17)$$

where $(\tau_*)_e$ is the effective bed shear stress, α_t and β_t are empirical coefficients, z_w is water surface elevation, and s is space vector along the sreamwise direction. Since superelevation of the water-surface occurs at the nose of the pier, Eq. (17) acts to locally increase the effective bed shear stress above the bed shear stress τ_* computed by the URANS model. In a similar study, Jia et al. [23] proposed an empirical formula that augments the local shear stress in the front of the pier by sensing the modest vertical downflow that URANS models typically yield in this region. According to this formulation, Eq. (15) is modified by adding a correction term to its right hand side as follows [23]:

$$T = \frac{\tau_* - \tau_{*cr}}{\tau_{*cr}} + \frac{C_s \widehat{\tau_*} \frac{w}{w_{max}}}{\tau_{*cr}} \quad (18)$$

where $C_s = 3.0$ is an empirical constant, $\widehat{\tau_*}$ is the spatial averaged bed shear stress around the pier, w is local mean vertical velocity component close to the bed, and w_{max} is the infinity norm of vertical velocity component around pier at the upper edge of the bed-load layer.

We evaluate the predictive capabilities of the correction proposed by Jia et al. [23] by implementing it to simulate the cylindrical and diamond shaped piers. More specifically, we replace in the model formulation Eq. (15) with the Eq. (18) and carry out calculations on the finest grid systems for each case (C_c and C_d).

Fig. 11 compares the measured and computed (by the Jia et al. formulation) scour pattern around the cylinder pier at equilibrium. The implemented correction obviously works well for this case in the front of the cylinder as it does predict a deeper scour hole that wraps around the entire front half of the cylinder as observed in the measurements. The accuracy of the predicted results, however, deteriorates significantly downstream of the cylinder where a non-physical, large, elongated deposition bar develops extending several cylinder diameters downstream. The computed deposition patterns in this region are in gross qualitative and quantitative dissagreement with the measurements.

The comparisons between experiments and simulations for the diamond pier are shown in Fig. 12 and reveal especially interesting trends. For this case, the performance of the model with the Jia et al. ad hoc correction deteriorates dramatically in the leading edge region of the pier relative to the baseline model without any correction (see Fig. 9). This is because the empirical formula senses the vertical downflow predicted by the URANS model and augments spuriously the mean bed shear stress yielding much deeper, than measured, scour that spans almost the entire upstream face of the pier.

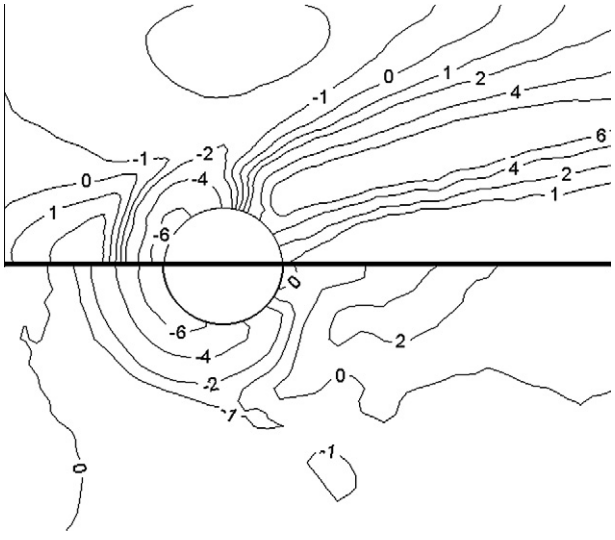

Fig. 11. Comparison of the measured bed elevation (bottom) and the bed elevation computed using the correction of Eq. (18) (top) for the diamond pier case (in cm). Computed results are shown for grid C_c. The flow direction is from left to right.

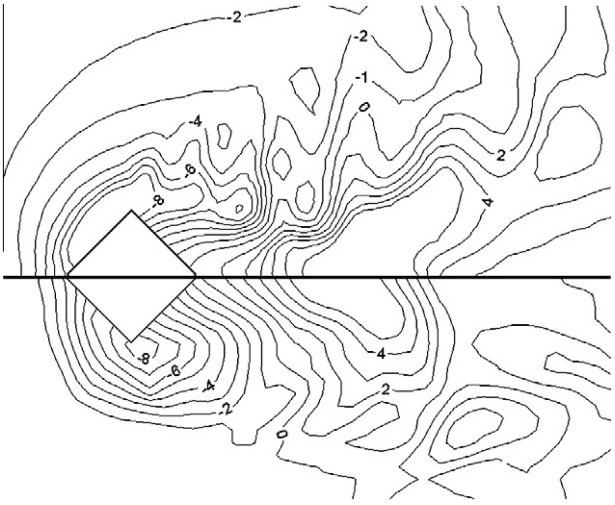

Fig. 12. Comparison of the measured bed elevation (bottom) and the bed elevation computed using the correction of Eq. (18) (top) for the diamond pier case (in cm). Computed results are shown for grid C_d. The flow direction is from left to right.

It is, therefore, evident from the results presented herein that the performance of the ad hoc correction of Jia et al. depends on both the geometry of the pier and the region of the flow. For cylindrical piers it yields non-physical results in the wake of cylindrical piers as well as in the leading edge region of sharp-edge piers like the diamond case.

7. Conclusions and discussion

We have carried out numerical simulations and laboratory experiments aimed at quantifying the predictive capabilities of the recently developed hydro-morphodynamic CURVIB method of Khosronejad et al. [26]. The method was applied to solve the URANS equations closed with the k-ω model with wall functions. Three pier geometries, a cylindrical, a square and a diamond, were studied to investigate the effect of pier bluntness on the dynamics of scour and the predictive capabilities of the model. For each case extensive grid refinement studies were carried out to investigate the effect of grid resolution on the accuracy of the numerical results. The results we presented herein show that the predictive capabilities of the URANS hydro-morphodynamic model we employ in this work do not depend on the grid resolution. The systematic grid refinement studies we carried out for all three cases have shown that the computed scour and deposition patterns, both in terms of maximum values and overall patterns, are insensitive to grid refinement. This finding points to the conclusion that the main culprit for the observed discrepancies between experiments and simulations should be the URANS turbulence model and/or the morphodynamic model we have employed in this work.

A rather striking finding of our work is that the predictive capabilities of our model depends on the details of the geometry of the studied pier cross-section. For example, we obtained excellent results for the diamond-shaped pier both in terms of the temporal evolution of scour and the overall spatial distribution patterns of scour and deposition. In contrast, for the cylindrical and square shapes the numerical model overpredicted the growth rate of scour and failed to capture the region of deep scour at the pier nose.

These findings should be attributed to the relative importance of the energetic THSV system as a scour inducing mechanism as function of pier nose geometry. It has already been shown, for instance, (see [51,16,9,10]) that the strength of the mean THSV and the intensity of the bi-modal THSV fluctuations depend critically on the details of the pier nose geometry and in particular on the so-called bluntness factor (BF) [16], which is proportional to the pier nose radius of curvature. Based on the definition given in [51], the BF in our case varies from infinity for the flat-nose square pier, to approximately 1.1 for the cylinder case, to zero for the sharp edge diamond pier. As shown by Olcmen and Simpson [37] the bi-modal fluctuations of the THSV diminish as the BF approaches zero and the intensity of the THSV system weakens to the point that it may be difficult to detect experimentally [51]. These experimental observations are very much consistent with the results of our scour experiments and our numerical simulations.

For the zero-bluntness diamond shaped pier the THSV is too weak, if at all present, and does not contribute to local scour. In this case, the local acceleration of the flow as it is redirected around the two side corners of the cross-section provides the only mechanism for increasing the bed shear stress about the critical value and inducing scour in the vicinity of the pier. The maximum scour for this case is confined in regions around the pier side corners and very little scour is observed at the pier nose (see Fig. 9). The local acceleration of the flow around the pier is a purely kinematic effect and for that it is resolved by the URANS model. As a result, the model produces equilibrium scour and deposition patterns and a temporal evolution of scour which are in very good agreement with the measurements. On the other hand, for the blunt square and cylindrical shapes the bi-modal THSV fluctuations are strong and give rise to large instantaneous and root-mean square (RMS) values of the bed shear stress at the pier nose [15,30]. These large instantaneous increments of bed shear stress combine with the local mean acceleration effect around the sides of the pier giving rise to a large scour hole of fairly uniform scour depth wrapping around the entire pier leading edge region.

As has also been shown in previous studies for cylindrical piers, isotropic URANS models are too diffusive to resolve the rich dynamics of the THSV system and for that fail to capture the region of deep scour at the pier nose [39,38]. There have been, however, numerical studies reported in the literature (see for example [1,23,60]) in which a URANS model was employed successfully to reproduce scour patterns around the cylindrical piers. Such models compensate for the inherent inability of the URANS hydrodynamic model to resolve the driving mechanism of scour at the pier nose (i.e. the intense fluctuations of the energetic THSV system) by adding an ad hoc correction in the morphodynamic model. We investigated the performance of one such correction (Jia et al. [23]) by carrying out simulations for the cylindrical and diamond pier shapes. Our results showed that such ad hoc corrections are not universal and need to to be applied with great caution since their predictive ability varies both with the shape of the pier and the region of the flow. While the correction improves the performance of the baseline URANS model in the leading edge region of the cylindrical pier, it yields spurious deposition patterns in the wake region. For the diamond shaped pier, the correction yields to non-physical scour at the front of the pier and drastically deteriorates the performance of the baseline model.

A major conclusion of our work is that the numerical prediction of scour past blunt-nose piers continues to remain a major challenge. Clearly URANS models are not adequate in that regard. Based on the recent results of Escauriaza and Sotiropoulos [15], hybrid URANS/LES or LES models that can resolve the rich dynamics of the THSV should be used as the building block hydrodynamic model for physics-based quantitative accurate simulations. As discussed in [15,41] several challenges do remain, however, for implementing such high-resolution models as predictive scour tools. These include: (1) the computational time and excessive computational resources such models require to reach equilibrium; and (2) the lack of quantitative physics-based criteria linking instantaneous transport processes at the bed with instantaneous flow properties near the bed. The former can be addressed by further advances in computational algorithms taking advantage of massively parallel computational platforms while the latter require new sophisticated experiments aimed at providing the much needed physical insights (see for example Diplas et al. [4]).

Acknowledgments

This work was supported by NSF Grants EAR-0120914 (as part of the National Center for Earth-Surface Dynamics) and EAR-0738726, National Cooperative Highway Research Program Grant NCHRP-HR 24-33, and a Grant from Yonsei University, South Korea, as part of the ECORIVER21 project. Computational resources were provided by the University of Minnesota Supercomputing Institute.

References

[1] Abbasnia AH, Ghiassi R. Improvements on bed-shear stress formulation for pier scour computation. Int J Numer Methods Fluids 2010. doi:10.1002/fld.2372.
[2] Agui JH, Andreopoulos J. Experimental investigation of a three dimensional boundary layer flow in the vicinity of an upright wall mounted cylinder. J Fluids Eng 1992;114:566–76.
[3] Ali KH, Karim O. Simulation of flow around piers. J Hydraul Res 2002;40(2):161–74.
[4] Apsilidis N, Diplas P, Dancey CL, Vlachos P, Raben SG. Local scour at bridge piers: the role of Reynolds number on horseshoe vortex dynamics. In: Proceedings of the fifth international conference on scour and erosion (ICSE-5).
[5] Baker C. The turbulent horseshoe vortex. J Wind Eng Indus Aerodyn 1980;6:9–23.
[6] Borazjani I, Ge L, Sotiropoulos F. Curvilinear immersed boundary method for simulating fluid structure interaction with complex 3D rigid bodies. J Comput Phys 2008;227:7587–620.
[7] Briaud JL, Ting F, Chen H, Cao Y, Gudavalli R, Perugu S, et al. Sricos: prediction of scour rate in cohesive soils at bridge piers. J Geo Geoenv Soc Am, ASCE 1999;125(4):237–46.
[8] Constantinescu G, Koken M. Time dependent and time averaged turbulence structure of flow past a surface mounted cylinder. In: Proceedings of 4th ICCHMT, Paris, France.
[9] Dargahi B. The turbulent flow field around a circular cylinder. Exp Fluids 1989;8:1–12.
[10] Dargahi B. Controlling mechanism of local scouring. J Hydraul Eng 1990;116(10):1197–214.
[11] Devenport WJ, Simpson RL. Time-dependent and time-averaged turbulence structure near the nose of a wing-body junction. J Fluid Mech 1990;210(2):23–55.
[12] Dey S, Bose S, Ghandikota LS. Clear water scour at circular piers: a model. J Hydraul Eng 1995;121(12):869–76.
[13] Doligalski TL, Smith CR, Walker JDA. Vortex interactions with walls. Ann Rev Fluid Mech 1994;26:573–616.
[14] Escauriaza C, Sotiropoulos F. Initial stages of erosion and bed-form development in turbulent flow past a bridge pier. J Geophys Res 2011;116:F03007.
[15] Escauriaza C, Sotiropoulos F. Lagrangian model of bed-load transport in turbulent junction flow. J Fluid Mech 2011;666:36–76.
[16] Fleming J, Simpson R, Devenport W. An experimental study of a turbulent wingbody junction flow. Exp Fluids 1993;14:366378.
[17] Ge L, Sotiropoulos F. 3d unsteady RANS modeling of complex hydraulic engineering flows. part i: Numerical model. J Hydraul Eng 2005;131(9):800–8.
[18] Ge L, Sotiropoulos F. A numerical method for solving the 3D unsteady incompressible Navier–Stokes equations in curvilinear domains with complex immersed boundaries. J Comput Phys 2007;225:1782–809.
[19] Gilmanov A, Sotiropoulos F. A hybrid cartesian/immersed boundary method for simulating flows with three-dimesional, geometrically complex, moving bodies. J Comput Phys 2005;207:457.
[20] Graf WH, Istiarto I. Flow pattern in the scour hole around a cylinder. J Hydraul Res 2002;40(1):13–9.
[21] Hager WH. Scour in hydraulic engineering. Water Manage 2007;160:159–68.
[22] Hussein H, Martinuzzi R. Energy balance for turbulent flow around a surface mounted cube placed in a channel. Phys Fluids 1996;8:764–80.
[23] Jia Y, Xu Y, Wang SY. Numerical simulation of local scouring around a cylindrical pier. In: Proceedings of ICSF-1, 1st international conference on scour of Fundations, Texas A&M University, Texas, USA.

[24] Kang S, Lightbody A, Hill C, Sotiropoulos F. High-resolution numerical simulation of turbulence in natural waterways. Adv Water Resour 2011;34(1):98–113.
[25] Kang S, Sotiropoulos F. Flow phenomena and mechanisms in a field-scale experimental meandering channel with a pool-riffle sequence: insights gained via numerical simulation. J Geophys Res 2011;116:F0301.
[26] Khosronejad A, Kang S, Borazjani I, Sotiropoulos F. Curvilinear immersed boundary method for simulating coupled flow and bed morphodynamic interactions due to sediment transport phenomena. Adv Water Resour 2011;34(7):829–43.
[27] Khosronejad A, Rennie C, Salehi A, Townsend R. 3D numerical modeling of flow and sediment transport in laboratory channel bends. J Hydraul Eng 2007;133(10):1123–34.
[28] Kirkil G, Constantinescu S. The horseshoe vortex systemaround a circular bridge pier on a flat bed. In: XXXIst International association hydraulic research congress, Seoul, Korea.
[29] Kirkil G, Constantinescu S, Ettema R. The horseshoe vortex system around a circular bridge pier on equilibrium scoured bed. In: World water and environmental resources congress, Alaska.
[30] Kirkil G, Constantinescu SG, Ettema R. Coherent structures in the flow field around a circular cylinder with scour hole. J Hydraul Eng 2008;134(5):572587.
[31] Kirkil G, Constantinescu SG, Ettema R. Detached eddy simulation investigation of turbulence at a circular pier with scour hole. J Hydraul Eng 2009;135(11):888–901.
[32] Martinuzzi R, Tropea C. The flow around surface-mounted, prismatic obstacles placed in a fully developed channel flow. J Fluids Eng 1993;115:85–92.
[33] Melville BW, Chiew YM. Time scale for local scour at bridge piers. J Hydraul Eng 1999;125(1):59–65.
[34] Mendoza-Cabrales C. Computation of flow past a cylinder mounted on a flat plate. In: ASCE Hydraulic engineering, proceedings of national conference.
[35] Nagata N, Hosoda T, Nakato T, Muramoto Y. Three-dimensional numerical model for flow and bed deformation around river hydraulic structures. J Hydraul Eng 2005;131(12):1074–87.
[36] Nurtjahyo PY. Numerical Simulation of Pier Scour and Contraction Scour, Ph.D. thesis, Department of Civil Engineering, Texas A&M University, Texas; 2002.
[37] Olcmen M, Simpson R. Influence of wing shapes on surface pressure fluctuations at wing-body junctions. AIAA J 1994;32:615.
[38] Olsen N, Kjellesvig HM. Three dimensional numerical flow modeling for estimation of maximum local scour depth. J Hydraul Res 1998;36(4):579590.
[39] Olsen N, Melaaen C. Three-dimensional calculation of scour around cylinders. J Hydr Eng 1993;119(9):1048–54.
[40] Paik J, Escauriaza C, Sotiropoulos F. On the bi-modal dynamics of the turbulent horseshoe vortex system in a wing-body junction. Phys Fluids 2007;19: 045107.
[41] Paik J, Escauriaza C, Sotiropoulos F. Coherent structure dynamics in turbulent flows past in-stream structures: Some insights gained via numerical simulation. J Hydraul Eng 2010;136(12):981–93.
[42] Paik J, Sotiropoulos F. Coherent structure dynamics upstream of a long rectangular block at the side of a large aspect ratio channel. Phys Fluids 2005;17:104–15.
[43] Paik J, Sotiropoulos F, Porte-Agel F. Detached Eddy Simulation of the flow around wall-mounted cubes in tandem. Int J Heat Fluid Fl 2009;30:286–305.
[44] Paola C, Voller VR. A generalized Exner equation for sediment mass balance. J Geophys Res 2005;110:F04014.
[45] Richardson JE, Panchang VG. Three-dimensional simulation of scour-inducing flow at bridge piers. J Hydraul Eng 1998;124(5):530–40.
[46] Rodi W. Comparison of LES and RANS calculations of the flow around bluff bodies. J Wind Eng Ind Aerodyn 1997;6971:5575.
[47] Roulund A, Sumer BM, Fredsoe J, Michelsen J. Numerical and experimental investigation of flow and scour around a circular pile. J Fluid Mech 2005;534:351–401.
[48] Salaheldin TM, Imran J, Chaudhry MH. Numerical modeling of three-dimensional flow field around circular piers. J Hydraul Eng 2004; 130(2):91100.
[49] Seal CV, Smith CR. Visualization of a mechanism for three-dimensional interaction and near-wall eruption. J Fluid Mech 1999;394:193–203.
[50] Selim Yalin M. River mechanics. Pergamon Press; 1992.
[51] Simpson RL. Junction flows. Ann Rev Fluid Mech 2001;33:415–43.
[52] Sumer BM. Mathematical modelling of scour: A review. J Hydraul Res 2007;45(6):723–35.
[53] Tseng MH, Yen CL, Song CCS. Computation of three-dimensional flow around square and circular piers. Int J Numer Methods Fluids 2000;34:207–27.
[54] Unger J, Hager WH. Down-flow and horseshoe vortex characteristics of sediment embedded bridge piers. Exp Fluids 2007;42(1):119.
[55] Van Rijn LC. Principles of sediment transport in rivers, estuaries, and coastal seas. Aqua Publications; 1993.
[56] Wilcox DC. Reassessment of the scale-determining equation for advanced turbulence models. AIAA J 1988;26:1299–310.
[57] Wilcox DC. Simulation of transition with two-equation turbulence model. Am Inst Aeronaut Astronaut J 1994;42(2):247–55.
[58] Wu W. Computational river dynamics. Taylor & Francis; 2008.
[59] Wu W, Rodi W, Wenka T. 3D numerical modeling of flow and sediment transport in open channels. J Hydraul Eng 2000;126(1):4–15.
[60] Wu W, Wang S. Prediction of local scour of non-cohesive sediment around bridge piers using FVM-based cche2d model. In: Proceedings of ICSF-1, 1st International conference on scour of fundations, Texas A&M University, Texas, USA.